International Journal of Fatigue 162 (2022) 107001

Contents lists available at ScienceDirect

International Journal of Fatigue

journal homepage: www.elsevier.com/locate/ijfatigue

Effect of load blocks on fatigue crack growth

D.M. Neto [a], E.R. Sérgio [a], M.F. Borges [a], L.P. Borrego [b], F.V. Antunes [a,*]

[a] Univ Coimbra, Centre for Mechanical Engineering, Materials and Processes (CEMMPRE), Department of Mechanical Engineering, Portugal
[b] Instituto Superior de Engenharia de Coimbra, Centre for Mechanical Engineering, Materials and Processes (CEMMPRE), Department of Mechanical Engineering, Portugal

ARTICLE INFO

Keywords:
Fatigue crack growth
Load blocks
Plastic deformation
Crack closure
Partial closure
Crack tip blunting

ABSTRACT

This research studies fatigue crack growth (FCG) in MT and CT specimens made of 6082-T6 aluminium alloy and Ti6Al4V, respectively, submitted to Low-High and High-Low load sequences. A numerical approach based on cumulative plastic strain at the crack tip was followed. A good agreement was found between numerical predictions and experimental results, which validate the assumption that cyclic plastic deformation is the main damage mechanism. Crack closure was able to explain the peak of da/dN in LH_{min} (Low-High blocks keeping the maximum load), the crack arrest in HL_{min} load pattern and the decrease of the influence of contact and non-contact conditions with the increase of stress ratio, R. The lack of material hardening is responsible for crack tip blunting which eliminates totally or partially the load history in LH_{min} patterns. Finally, partial crack closure is observed in high-low load blocks, due to the plastic wake of the first load block, which reduces FCG and may even arrest the crack, particularly in HL_{min} patterns.

1. Introduction

Design against fatigue based on damage tolerance approach requires the knowledge of fatigue crack growth (FCG) rate, which is very sensitive to load history. Real components and structures are typically submitted to complex loading patterns, with constant amplitude loadings being of purely theoretical interest. Different standard load patterns have been proposed like TWIST and FALSTAFF sequences for transport and fighter aircraft, respectively, or CARLOS for automotive applications [1]. The TWIST load spectrum [2], for example, has an average of a thousand small gust cycles per flight with a major cycle associated with the ground-air-ground sequence and a few overloads associated with more severe atmospheric turbulence. However, there is a great complexity associated with these standard load patterns and with real patterns, and it is recommended to start studying simpler patterns for a progressive understanding of the fundamental mechanisms.

In a strategy of increasing complexity, it is natural to consider in a first approach the study of overloads, underloads and load blocks. The overloads have been widely studied considering experimental, numerical and analytical approaches. Different mechanisms have been proposed to explain the effect of this Variable Amplitude Loading (VAL), namely crack tip blunting [3,4], residual stresses [4,5,6], strain hardening [7,8], crack branching [9] and plasticity induced crack closure [10–12]. In a previous work [12], it was found that the typical transient behavior following overloads is mainly linked to crack closure phenomenon, while the residual stresses have a minor effect. In fact, the elimination of the contact of crack flanks in the numerical models had no effect on residual stresses but had a dramatic effect on da/dN, removing the transient behaviour. The effect of load blocks is less studied. Ward-Close *et al.* [13] attributed the effect of load blocks to changes in the degree of closure in the wake of the crack. Sehitoglu and McDiarmid [14] studied the effect of a decrease in stress range on FCG in mild steel plate. The delay period was found to be a function of load step-down ratio and specimen thickness. The crack extension affected by retardation was related to the plastic zone size associated with the initial high stress level. Borrego *et al.* [15] pointed out the importance of plasticity induced crack closure. Partial closure was used to explain the trends observed in High-Low load patterns. On the other hand, Remadi *et al.* [16] predicted the effect of load blocks using the Unigrow model proposed by Noroozi and Glinka [17]. This approach is based on the residual stresses ahead of crack tip instead of crack closure. Therefore, the fundamental mechanisms behind the effect of load blocks are not completely understood.

Numerical studies are very interesting to identify the fundamental mechanisms behind FCG, in addition to being ideal for developing parametric studies. Crack tip plastic deformation is usually assumed to

* Corresponding author. Tel.: 00351 239790700; fax: 00351239790701.
E-mail address: fernando.ventura@dem.uc.pt (F.V. Antunes).

https://doi.org/10.1016/j.ijfatigue.2022.107001
Received 1 March 2022; Received in revised form 4 May 2022; Accepted 7 May 2022
Available online 13 May 2022

be the main mechanism behind FCG [18,19]. Since crack tip damage is non-linear and irreversible, it is recommendable to use non-linear parameters as crack driving force, instead of the linear elastic ΔK parameter. Different parameters have been proposed, namely the CTOD [20], the plastic CTOD [21], ΔJ [22–24], the dissipated energy [25], the cumulative plastic strain [26] and the size of monotonic plastic zone [27]. However, the numerical models must be validated with experimental results to prove their ability to simulate FCG phenomenon. In fact, there is a natural distrust regarding the ability of numerical approaches to replicate the complexity of physical phenomena, namely the propagation of cracks due to fatigue.

Therefore, this research studies the transient effects observed in Low-High and High-Low load sequences. A numerical approached based on cumulative plastic strain was followed to predict FCG in CT and MT specimens. The main objectives of this work are: (ii) validate the numerical approach with experimental results for load blocks applied in MT specimens made of 6082-T6 aluminium alloy; (ii) understand the mechanisms responsible for the effect of load blocks, therefore achieving a better understanding of VAL. Models with and without contact of crack flanks were considered to isolate the effect of crack closure phenomenon. The materials studied were the 6082-T6 aluminium alloy and the Ti6Al4V titanium alloy.

2. Numerical model

The numerical simulations of FCG were performed using the in-house finite element code DD3IMP [28]. The numerical model considers the elasto-plastic behavior of the specimen, assuming the mechanical behavior isotropic. Two different geometries are adopted for the specimens, namely the middle-crack tension (MT) specimen and the Compact Tension (CT) specimen, whose geometry and dimensions are according to ASTM E647 [29]. The main dimensions of each specimen are presented in Fig. 1. Due to the symmetry conditions, only one quarter of the MT specimen is modelled, while only the upper part of the CT specimen was simulated. In both cases, plane stress conditions are assumed in the numerical simulation, as indicated in Fig. 2b. The contact of the crack flanks is simulated using a rigid surface at the symmetry plane, which can be removed to eliminate the crack closure effect [30]. The specimen thickness used in the numerical model was 0.1 mm.

In Fig. 2a is represented the finite element mesh of the CT specimen that comprised 7287 3D linear hexahedral isoparametric elements and 14,918 nodes. At the crack tip, an ultra-refined mesh (Fig. 2c and 2d) was implemented, constituted by square elements with 8 × 8 μm^2, aiming to accurately quantify strain gradients and local stress. This size dictates the value of the crack propagation increment. Only one layer of elements was considered along the thickness, therefore the size of elements along this direction was 0.1 mm. The region with refined meshed was shifted in accordance with the initial crack length.

Two different materials are studied according to the specimen geometry. The MT specimen is composed by the 6082 aluminum alloy with T6 heat treatment, while the material of the CT specimen is the titanium alloy Ti6Al4V produced by selective laser melting process. For both materials, the elastic behavior is assumed isotropic and described by the Hooke's law. The plastic behavior is assumed isotropic (von Mises), while the work hardening of the aluminum alloy and the titanium alloy is given by the Voce and Swift law, respectively. The flow stress defined by the Voce hardening law is given as follows:

$$Y = Y_0 + (Y_{Sat} - Y_0)[1 - exp(-C_Y \bar{\varepsilon}^p)] \quad (1)$$

where Y_0 is the yield stress, Y_{Sat}, and C_Y are material parameters of the Voce law and $\bar{\varepsilon}^p$ is the equivalent plastic strain. Regarding the Swift hardening law, the flow stress is given as follows:

$$Y = K\left[\left(\frac{Y_0}{K}\right)^{\frac{1}{n}} + \bar{\varepsilon}^p\right]^n \quad (2)$$

where K and n are material parameters of the Swift law. In order to take into account the strain ratchetting, the kinematic hardening model of Armstrong and Frederick was adopted, which is given by:

$$\dot{X} = C_X\left[X_{Sat}\frac{\sigma' - X}{\bar{\sigma}} - X\right]\dot{\bar{\varepsilon}}^p \quad (3)$$

where C_X and X_{Sat} are the material parameters of Armstrong-Frederick law, σ' is the deviatoric stress of the Cauchy stress tensor, $\boldsymbol{X}$ is the back stress tensor, $\bar{\sigma}$ is the equivalent stress and $\dot{\bar{\varepsilon}}^p$ is the equivalent plastic strain rate.

Table 1 presents the parameters of the elasto-plastic constitutive model for each material, which were obtained fitting numerical stress–strain curves to experimental data obtained from low-cycle fatigue tests [31,32]. A relatively large number of load cycles is considered, more than 50, therefore the material model simulates adequately the cyclic behavior of the material.

Regarding the MT specimen, the cyclic loading was applied remotely at the end of the specimen. On the other hand, in the CT specimen the load was applied at the upper nodes of the hole, avoiding to modelling of the pin. Both specimens were subjected to High-Low and Low-High block loading sequences to analyze the fatigue crack growth under block loading sequences. For the MT specimen the loading range was adjusted to achieve a constant value of ΔK, namely the baseline levels of 6, 9 and 12 MPa.m$^{1/2}$ and two different stress ratios, R = 0.05 and R = 0.4. Table 2 presents the magnitude of the applied load for each load block sequence applied in the CT specimen, which is schematically presented in Fig. 3. In the case of Low-High sequences, the only difference between LH_{min} and LH_{max} is the stress ratio of the first block, which is $R = 0.05$ and $R = 0.36$ in the LH_{min} and LH_{max}, respectively. Regarding the High-Low sequences, the only difference between HL_{min} and HL_{max} is the stress ratio of the second block, which is $R = 0.05$ and $R = 0.36$, respectively.

Crack propagation occurs by releasing the boundary condition of the crack tip element, i.e., the crack tip node is debonded at the instant of minimum load. The adopted fatigue crack growth criterion is based on cumulative plastic deformation assessed numerically at the crack tip

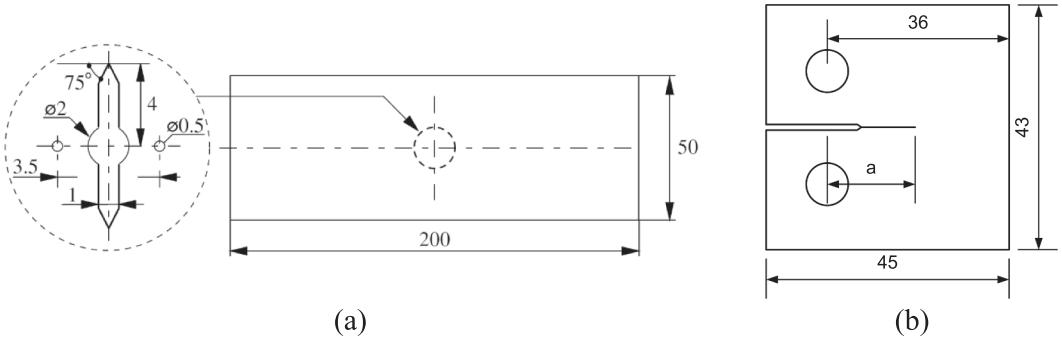

Fig. 1. Geometry and main dimensions [mm] of the: (a) MT specimen; (b) CT specimen.

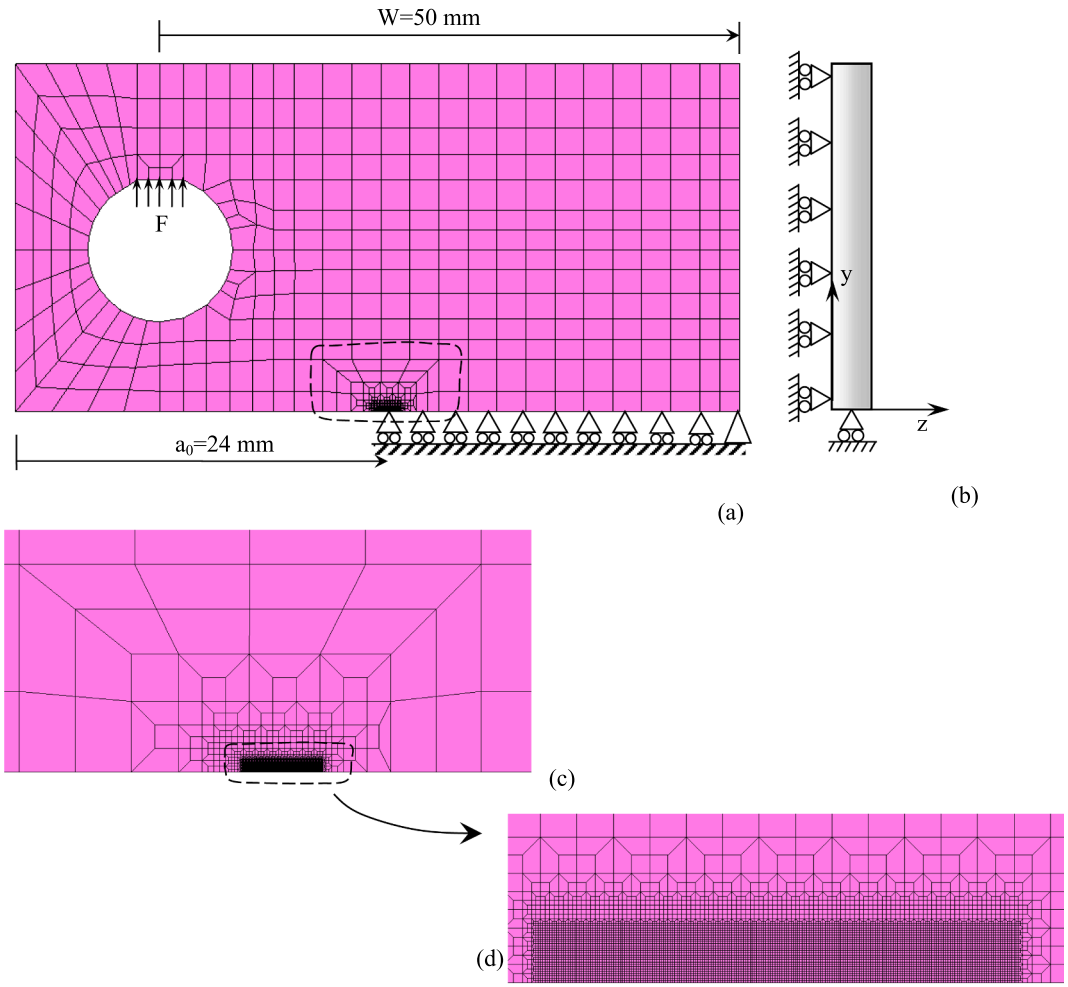

Fig. 2. Model of the C(T) specimen. (a) Load and boundary conditions. (b) Boundary conditions for plane stress state. (c) and (d) Details of finite element mesh.

Table 1
Elasto-plastic properties of the 6082 aluminum alloy and the titanium alloy Ti6Al4V.

Material	E [GPa]	ν	Y_0 [MPa]	Y_{sat} [MPa]	C	C_X	X_{sat} [MPa]
AA6082-T6 [31]	70	0.33	238.15	487.52	0.01	244.44	83.18
Material	E [GPa]	ν	Y_0 [MPa]	K [MPa]	n	C_X	X_{sat} [MPa]
Ti6Al4V [32]	115	0.33	823.5	707.1	−0.029	104.3	402.0

Table 2
Definition of the load sequences adopted in CT specimen.

Load sequence	F_{min} (1st block) [N]	F_{max} (1st block) [N]	F_{min} (2nd block) [N]	F_{max} (2nd block) [N]
Low-High (LH_{min})	2.2	44.05	2.2	65
Low-High (LH_{max})	23.15	65	2.2	65
High-Low (HL_{min})	2.2	65	2.2	44.05
High-Low (HL_{max})	2.2	65	23.15	65

[26], which is compared with a critical value, defining the load cycle at which the crack propagation occurs. Therefore, the predicted FCG rate is the ratio between the crack increment (8 μm) and the number of load cycles required to achieve the critical value of cumulative plastic strain at the crack tip.

Since the numerical predictions depend directly on the selected critical value of cumulative plastic strain, it is calibrated for each material studied. The idea behind the calibration procedure is to reduce the difference between numerical and experimental FCG rate, using a single value of FCG rate measured experimentally under constant amplitude loading. For this aluminum alloy, the calibration was carried out for $\Delta K = 9$ MPa.m$^{1/2}$ and $R = 0.05$, using different values for the critical plastic strain, which provide different values of FCG rate. Then, the critical value of cumulative plastic strain was obtained by interpolation of the numerical FCG rate over the experimental value. The obtained value was 261%. For the titanium alloy, the calibration of the critical value of plastic strain was performed in a previous work [32], having obtained the value of 153%.

3. Validation with experimental results

3.1. Experimental work

The validation of the numerical model using experimental data is carried out for the 6082-T6 aluminium alloy with the chemical

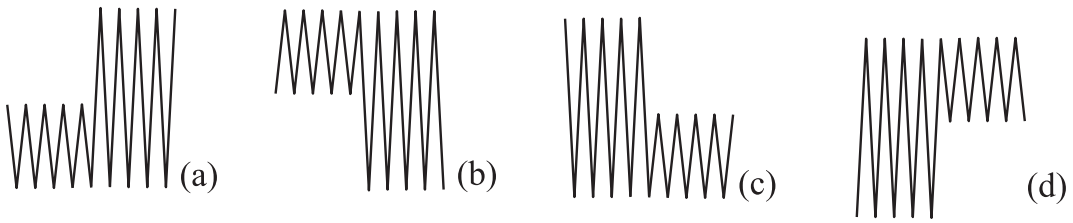

Fig. 3. Load patterns applied in the CT specimen: (a) Low-High sequence fixing the minimum load (LH_{min}); (b) Low-High sequence fixing the maximum load (LH_{max}); (c) High-Low sequence fixing the minimum load (HL_{min}); (d) High-Low sequence fixing the maximum load (HL_{max}).

composition shown in Table 3. The MT specimens were obtained in the longitudinal transverse (LT) direction from a laminated plate. The specimens with a thickness of 3 mm were tested at room temperature, in air, under constant amplitude loading using a hydraulic testing machine with a loading frequency of 15 Hz. Fig. 4 shows a MT specimen being tested, with a pin extensometer for crack closure measurements. The crack length, *a*, was obtained by optical measurement of crack tip position using of a travelling microscope (45 ×) attached to a micrometer. The crack growth rates were determined from the *a* versus *N* results, being *N* the number of load cycles, using the secant method proposed in ASTM E647 standard [29]. The influence of the load blocks was investigated under High–Low (HL) and Low–High (LH) sequences, at ΔK baseline levels of 6, 9 and 12 MPa $m^{1/2}$, at a stress ratio R = 0.05. More details of the experimental work may be found in Borrego *et al.* [15].

The Low–High sequence (Fig. 5a) produces an acceleration of crack growth rate, above the steady state level expected for the high block, followed by a gradual reduction to the steady-state corresponding to ΔK_2 level. The increase of ΔK jump extends the transient regime, as could be expected. These trends are consistent with the behaviour usually reported in the literature [13,14,33].

Fig. 5b shows the results obtained for the High-Low load blocks. For similar decrease of ΔK (12–9 versus 9–6 $MPam^{0.5}$), the transient regime is larger when the initial ΔK is higher, which is explained by the larger plastic zone, and the minimum da/dN is higher. The comparison with Fig. 5a indicates that transient regimes resulting from High-Low blocks are much more extensive for those obtained for Low-High blocks. For the load step from $\Delta K_1 = 12$ to $\Delta K_2 = 6$ MPa $m^{1/2}$ (not presented) the crack was arrested. This arrest is according Sehitoglu and McDiarmid [14], who observed non-propagating cracks in mild steel for load step ratios, $\Delta K_2/\Delta K_1$, less than 0.6. Micone and Waele [34] also observed arrest, but for $\Delta K_2/\Delta K_1$ less than about 0.4 in high strength offshore steel grades.

3.2. Numerical results

The comparison between predicted and experimental FCG rate in load blocks with stress ratio R = 0.05 is presented in Fig. 6 for two different cases: (a) Low-High load block with $\Delta K_1 = 9$ MPa.$m^{1/2}$ and $\Delta K_2 = 12$ MPa.$m^{1/2}$; (b) High-Low load block with $\Delta K_1 = 12$ MPa.$m^{1/2}$ and $\Delta K_2 = 9$ MPa.$m^{1/2}$. Fig. 7 presents similar results for Low-High load blocks with $\Delta K_1 = 6$ MPa.$m^{1/2}$ and $\Delta K_2 = 9$ MPa.$m^{1/2}$. The comparison between predicted and experimental FCG rate is carried out for two values of stress ratio, namely R = 0.05 in Fig. 7a and R = 0.4 in Fig. 7b.

The numerical results are globally in agreement with the experimental measurements, which is a good indication for the robustness of the numerical approach. The assumption that cyclic plastic deformation is the driving force for FCG is reinforced by these results. Note that the numerical model also includes the effects of plasticity induced crack closure, material hardening, residual stresses and crack tip blunting. The assumption of plane stress made in the numerical simulation is adequate for the thickness (t = 3 mm) of the specimens used in the experimental work. A good performance of the FCG simulation based on cumulative plastic strain was also observed in previous works of the authors. Borges *et al.* [26] successfully predicted the effect of ΔK observed experimentally in AA2024-T251 and 18Ni300 steel, while Neto *et al.* [12] predicted reasonably the effect of stress ratio, and Neto *et al.* [35] predicted correctly the effect of Superblock2020 load pattern.

All numerical curves in Figs. 6 and 7 show an initial decrease of numerical FCG rate before stabilization, during the first loading block,

Fig. 4. Experimental set-up for FCG test using a MT specimen.

Table 3
Chemical composition of the 6082-T6 aluminium alloy (wt.%).

Aluminium alloy	Al	Cu	Cr	Mg	Mn	Ti	Si	Fe	Zn
6082-T6	Bal.	0.04	0.01	0.8	0.68	0.01	1.05	0.26	0.02

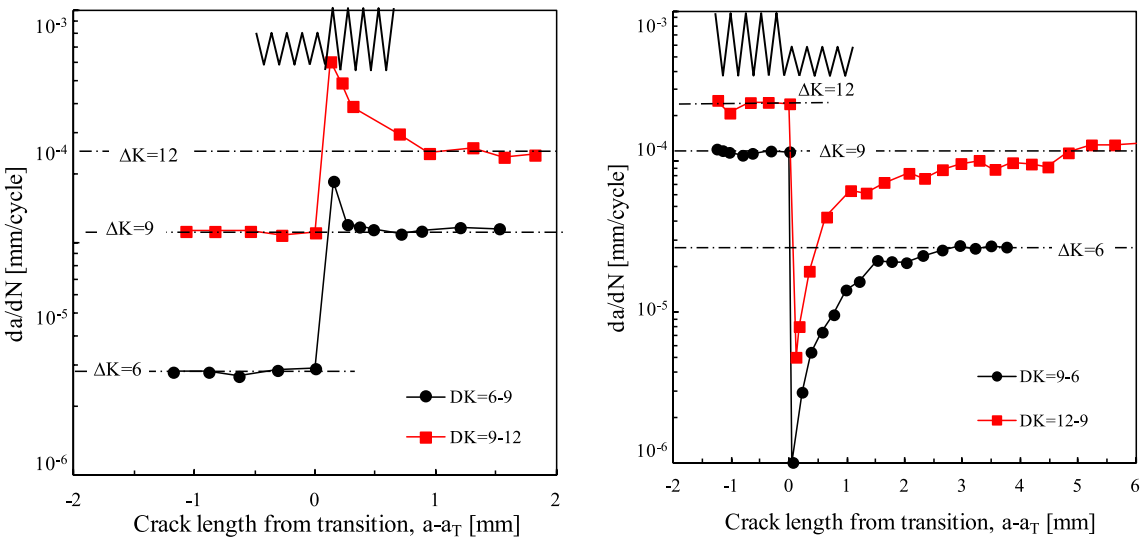

Fig. 5. Effect of load blocks on FCG rate for the 6082-T6 aluminium alloy. (a) Low-High. (b) High-Low.

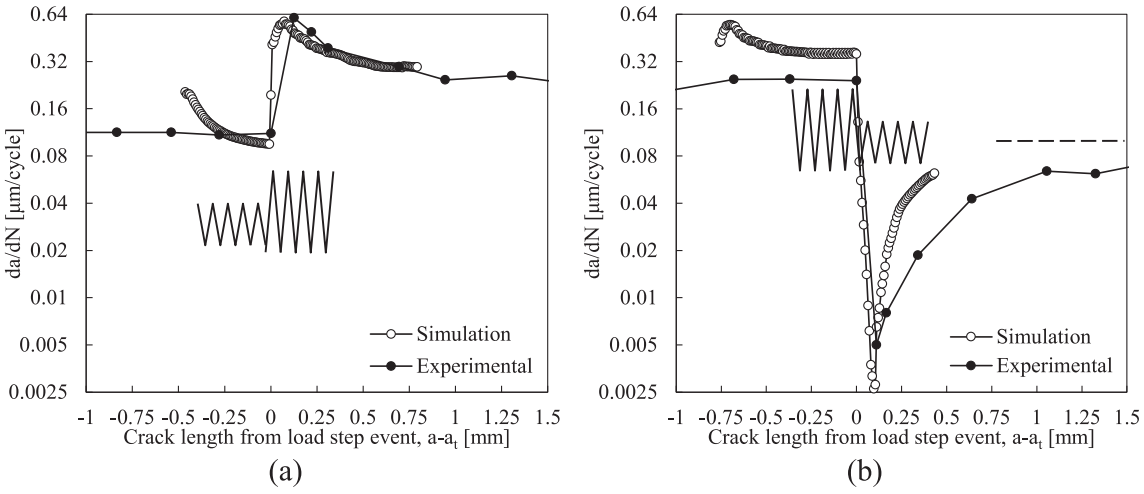

Fig. 6. Evolution of FCG rate in load blocks with R = 0.05: (a) Low-High load block with $\Delta K_1 = 9$ MPa.m$^{1/2}$ and $\Delta K_2 = 12$ MPa.m$^{1/2}$; (b) High-Low load block with $\Delta K_1 = 12$ MPa.m$^{1/2}$ and $\Delta K_2 = 9$ MPa.m$^{1/2}$.

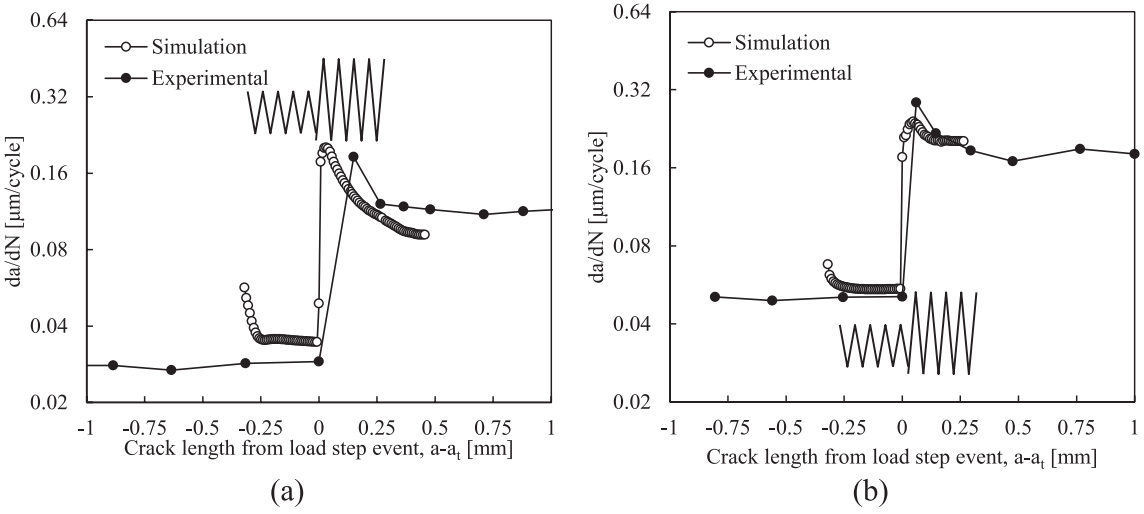

Fig. 7. Influence of the stress ratio on the FCG rate evolution in Low-High load blocks with $\Delta K_1 = 6$ MPa.m$^{1/2}$ and $\Delta K_2 = 9$ MPa.m$^{1/2}$: (a) R = 0.05; (b) R = 0.4.

which is related to plastic wake development. Fig. 6a shows an acceleration after block transition, leading to the maximum crack growth rate, which is about twice the value after stabilization. This peak and subsequent stabilization to the constant amplitude FCG rate are also observed in Fig. 7a and 5b, for other values of ΔK and stress ratio. The numerical/ experimental differences at the beginning of the second block may be explained by the relatively small number of measurement points in the experimental work. Anyway, the effects of loading parameters are all respected, namely the global increase of the FCG rate with the increase of the stress ratio observed in the comparative analysis of Fig. 7a and 7b.

In the High-Low block sequence (Fig. 6b), significant crack growth retardation is observed after the transition, followed by a progressive increase towards the constant amplitude da/dN value. Note that the initial acceleration due to the Low-High sequence is much lower than the retardation induced by the corresponding High-Low block analysed. All these trends were observed numerically. However, the extent of retardation is underestimated by the numerical model. This may eventually be attributed to other damage mechanism apart from cyclic plastic deformation.

4. Fundamental mechanisms behind the effect of load blocks

4.1. Effect of contact of crack flanks

Based on previous studies [10,12] for variable amplitude load sequences, crack closure is expected to have a strong impact on the FCG rate for load blocks. The numerical model can be used to isolate the effect of crack closure by artificially removing the contact of crack flanks. Note that this interesting numerical trick cannot be done experimentally.

Fig. 8 presents the evolution of the predicted FCG rate for the Low-High (LH) load blocks listed in Table 2 for the Ti6Al4V alloy, comparing the situation with and without contact at the crack flanks. Since the FCG rate predicted by the model that neglects the contact of the crack flanks is globally higher, the relative crack length ($a - a_t$) is adopted to simplify the comparison, where a_t denotes the crack length at the transition between loading blocks. Fig. 8a presents the FCG rate predicted for the LH_{min} load pattern (F_{min} identical in both blocks), highlighting the importance of the contact conditions in the crack flanks. The initial decrease of da/dN with crack propagation, also observed in Figs. 6 and 7, only occurs if the contact of the crack flanks is considered. Therefore, it is linked to crack closure phenomenon and is due to the formation of residual plastic wake. The transient behaviour observed after the transition between load blocks extents approximately 0.3 mm, obtaining da/dN = 0.4 μm/cycle in the steady state regime. However, without contact of crack flanks there is no transient regime and da/dN increases progressively with crack growth almost immediately after the transition. The stabilized da/dN values of the second load block show a great effect of contact of crack flanks, which can only be attributed to plasticity induced crack closure. The comparison with Fig. 6a and 7a (also for R = 0.05) indicates that the transient regime at the beginning of the second block is less extensive for the titanium alloy comparatively with the AA6082-T6, which is linked to lower plastic deformation levels.

The FCG rate predicted for the LH_{max} load pattern (F_{max} identical in both blocks) is presented in Fig. 8b. Since the stress ratio of the first block was substantially increased from R = 0.05 (LH_{min}) to R = 0.36 (LH_{max}), the difference between contact and non-contact conditions was strongly reduced. This indicates that there is almost no crack closure in the first load block due to the relatively high stress ratio. Besides, the transient regime was shortened (0.05 mm of extent), where the predicted da/dN shows a sudden increase until achieve approximately 0.4 μm/cycle. Neglecting the contact between the crack flanks, the effect of the stress ratio vanishes and consequently the evolution of the predicted FCG rate in LH_{min} and LH_{max} load patterns is identical, as can be seen comparing Fig. 8a and Fig. 8b.

The evolution of the predicted FCG rate for both High-Low load blocks listed in Table 2 is presented in Fig. 9, comparing the situation with and without contact at the crack flanks. The first load block of the load pattern HL_{min} and HL_{max} are identical. Neglecting the contact between the crack flanks, the predicted da/dN shows a gradual increase during the first load block. On the other hand, a transient behaviour is observed for da/dN at the beginning of the crack propagation when the contact of the crack flanks is considered. The extension of this transient regime is about 0.3 mm, after which the da/dN reaches approximately 0.4 μm/cycle. This is the FCG rate associated to the steady state regime of the second block in the load patterns LH_{min} and LH_{max} (see Fig. 8).

After the block transition, considering the HL_{min} load pattern (F_{min} identical in both blocks), the crack stops after the transition between loading blocks, i.e., the value of da/dN converges to zero, as shown in Fig. 9a. This behaviour was also observed experimentally for this load pattern [15]. Nevertheless, removing the contact between the crack flanks, da/dN shows a sudden decrease until it achieves approximately 0.2 μm/cycle after 0.05 mm of crack extension. This is the FCG rate previously obtained in the first block of the load pattern LH_{min} and LH_{max}, when the contact was neglected (see Fig. 8). Therefore, the crack stops only due to crack closure phenomenon. Since the stress ratio of the second block increased from R = 0.05 in HL_{min} to R = 0.36 in HL_{max}, the FCG rate presents a transient regime followed by a steady state evolution, as shown in Fig. 9b. Assuming the contact between the crack flanks,

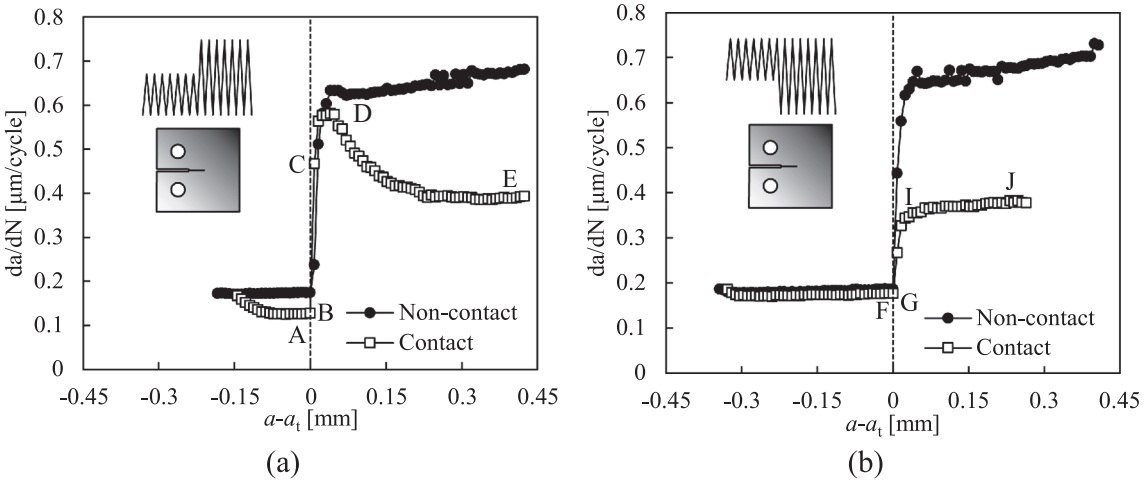

Fig. 8. Predicted FCG rate for two different Low-High load blocks, comparing the situation with and without contact of crack flanks: (a) LH_{min} load pattern; (b) LH_{max} load pattern. (Ti6Al4V).

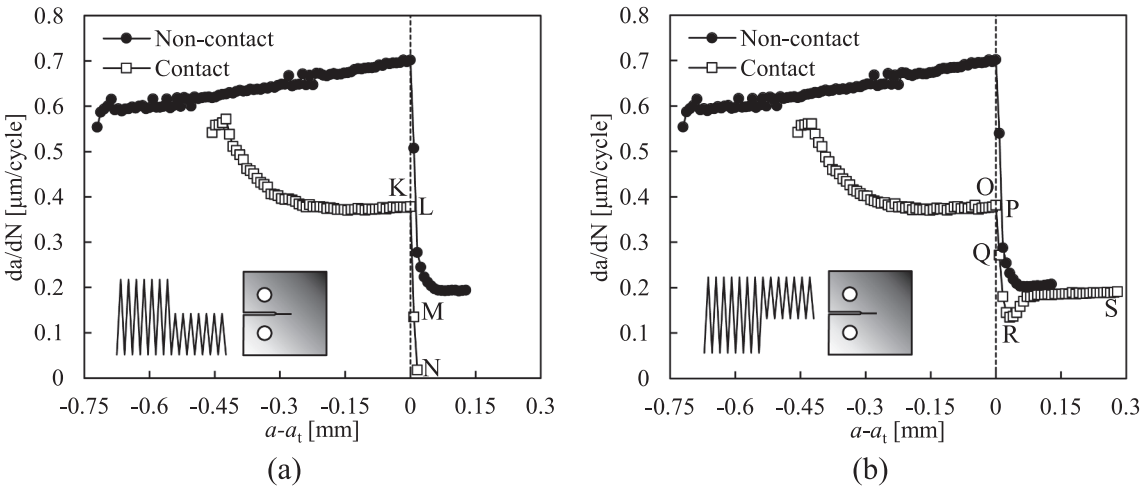

Fig. 9. Predicted FCG rate for two different High-Low load blocks, comparing the situation with and without contact of crack flanks: (a) HL_{min} load pattern; (b) HL_{max} load pattern.

the predicted da/dN shows a sudden decrease in the transition between loading blocks, reaching a minimum at some point ahead of the transition. Then, da/dN increases gradually to the constant amplitude FCG rate. Without contact, there is only a progressive decrease of da/dN after the block transition. Interestingly, the extent of this transient regime is approximately 0.05 mm, either considering or not the contact between the crack flanks.

The predicted crack tip profile for the HL_{min} load pattern is presented in Fig. 10a for three different values of applied force corresponding to the last load cycle. The length of crack closure at the minimum load is very extensive, being larger than 0.4 mm. Since the crack is arrested at the beginning of the second block (see Fig. 9a), the contact of crack flanks occurs mainly in the zone corresponding to the first load block. Thus, the residual plastic wake created during the first block is responsible by the arrest of the crack in the second block. This is partial closure, also named discontinuous closure, consisting of the contact of the crack flanks behind the crack tip while the current crack tip is still open. According to Paris *et al.* [36] and Kujawski [37] this remote contact of the crack flanks has an effect on the fatigue crack growth, therefore a correction to the crack closure concept is required. Borrego *et al.* [15] found a good correlation between crack closure and crack growth transients in block loading when the partial closure phenomenon was correctly account for.

Considering the HL_{max} load pattern, the predicted crack tip profile for three different values of applied force corresponding to the last load cycle is presented in Fig. 10b. The crack tip profile in the zone corresponding to the beginning of the second block contains a narrowing down zone, which induces contact closure. Indeed, the extent of this zone is approximately 0.05 mm, which is the range of the transient regime in the predicted da/dN, as shown in Fig. 9a. Thus, the transient decrease of the da/dN at the beginning of the second load block is caused by the contact between the crack flanks, disappearing when the contact between the crack flanks is neglected in the simulation.

Fig. 11a compares all results obtained for the Ti6Al4V with contact of crack flanks. There is always a transient regime after block transition and in one of the cases the crack even stops (HL_{min}). The largest transient regime is obtained for the LH_{min} situation, which also produces a significant peak of da/dN. Considering the loading sequences LH_{min} and LH_{max}, the FCG rate converge to the same value (0.4 µm/cycle) after the stabilization in the second block since both the stress ratio and the loading amplitude of the second block are identical. Besides, assuming steady state conditions, the FCG rate in the first (second) block of the loading sequence LH_{max} is identical to the one obtained in the second (first) block of the loading sequence HL_{max}.

Fig. 11b compares the situations without contact of crack flanks. There is no effect of the position of the smallest block, i.e., the results are the same independently of keeping the maximum or the minimum load in both blocks. The transition is significantly smaller, comparatively to

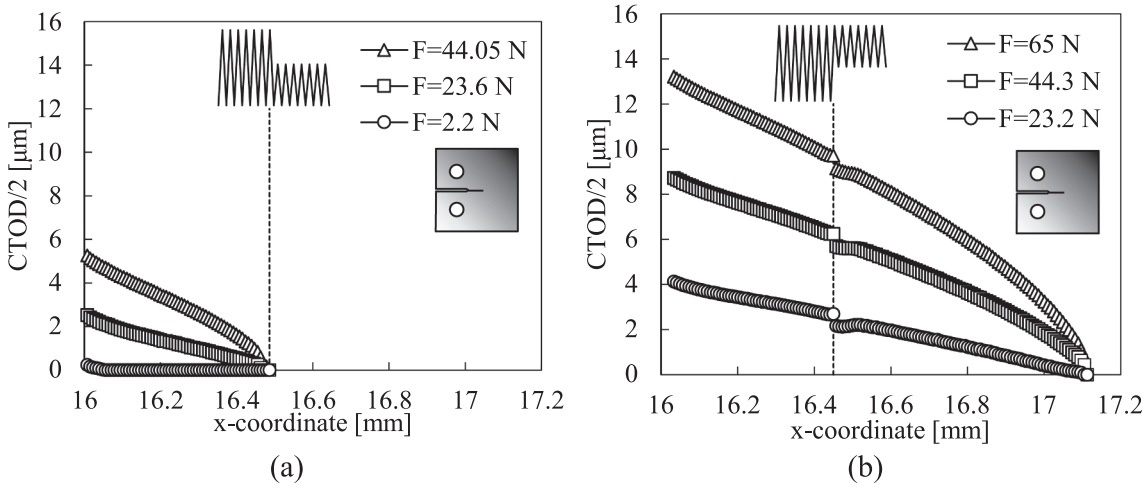

Fig. 10. Predicted crack tip profiles for two different High-Low load blocks at three different values of applied force: (a) HL_{min} load pattern; (b) HL_{max} load pattern.

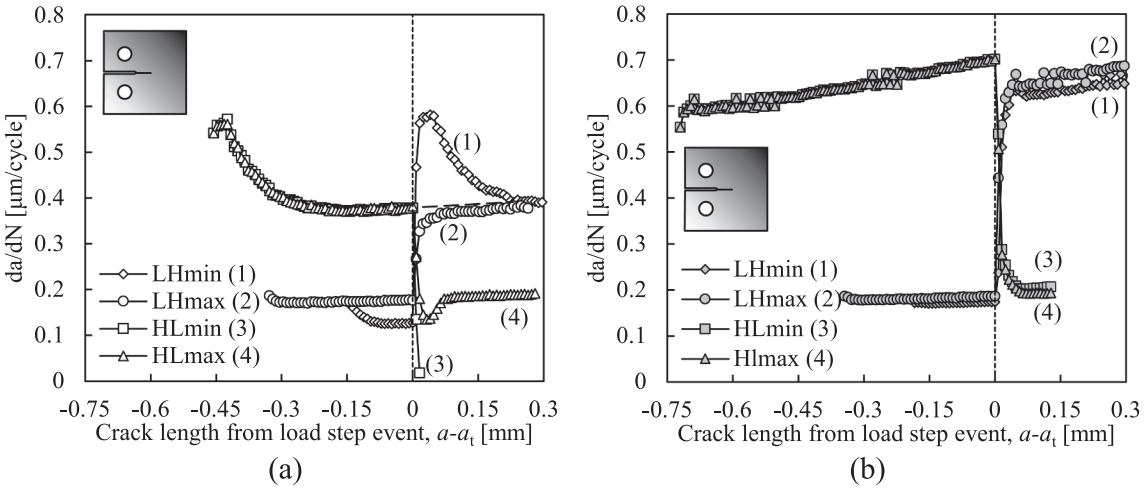

Fig. 11. Predicted FCG rate for different High-Low and Low-High block loading sequences: (a) with contact between the crack flanks; (b) without contact between the crack flanks.

the situations with contact of crack flanks. Anyway, there is a small transient region of about 50 µm. Only two stabilized levels of FCG rate are observed because only two amplitudes of loading are involved in the loading sequences studied.

4.2. CTOD plots

The CTOD plots are very interesting to understand what is happening at the crack tip. Fig. 12 plots CTOD versus load curves for the LH_{min} situation. The CTOD was assumed to be the vertical displacement of the first node behind current crack tip. The letters corresponding to each curve are indicated in Fig. 8a. The increase of load above the maximum load of the first block, indicated by the vertical dashed line in Fig. 12a, produces a relatively high increase of CTOD. The associated increase of plastic CTOD produces the blunting of crack tip, which eliminates the effect of previous residual plastic wake. This explains the absence of crack closure in curves C and D. Therefore, the lack of material hardening at the beginning of the second block plays a significant role. As the new residual plastic wake is formed, the CTOD decreases and crack closure regains its relevance (curve E in Fig. 12b).

Fig. 13 plots the CTOD curves for the LH_{max} situation, being the crack lengths defined by the letters indicated in Fig. 8b. The first load block has no crack closure, i.e., the CTOD is higher than zero even for the minimum load, which is a consequence of the relatively high stress ratio. The decrease of minimum load, at the beginning of the first block, produces crack closure, but the effective load range is not greatly affected. As the crack propagates, there is a decrease of crack closure level and therefore an increase of effective load range and da/dN.

Fig. 14 represents the CTOD plots for the HL_{min} situation. The crack lengths corresponding to the different letters are indicated in Fig. 9a. The decrease of maximum load reduced significantly the effective load range, and therefore the plastic CTOD (Fig. 14a). The propagation of the crack increases significantly the crack closure up to a point where the CTOD is totally elastic and there is no crack growth, i.e., the crack is arrested (Fig. 14b). In fact, curve N shows that after opening there is only elastic deformation, which is not supposed to propagate the crack.

Fig. 15 represents the CTOD plots for the HL_{max} situation, being the crack lengths corresponding to the letters indicated in Fig. 9b. The increase of minimum load eliminates immediately the crack closure level (Fig. 15a) and also a portion of the effective load range, which explains the reduction of da/dN. As the crack propagates there a quick movement of curve Q to curve R, which corresponds to the minimum da/dN, where some crack closure is visible. This crack closure is produced by the shape of the crack tip profile in the zone corresponding to the beginning of the second block (see Fig. 10b), disappearing with crack growth (curve S).

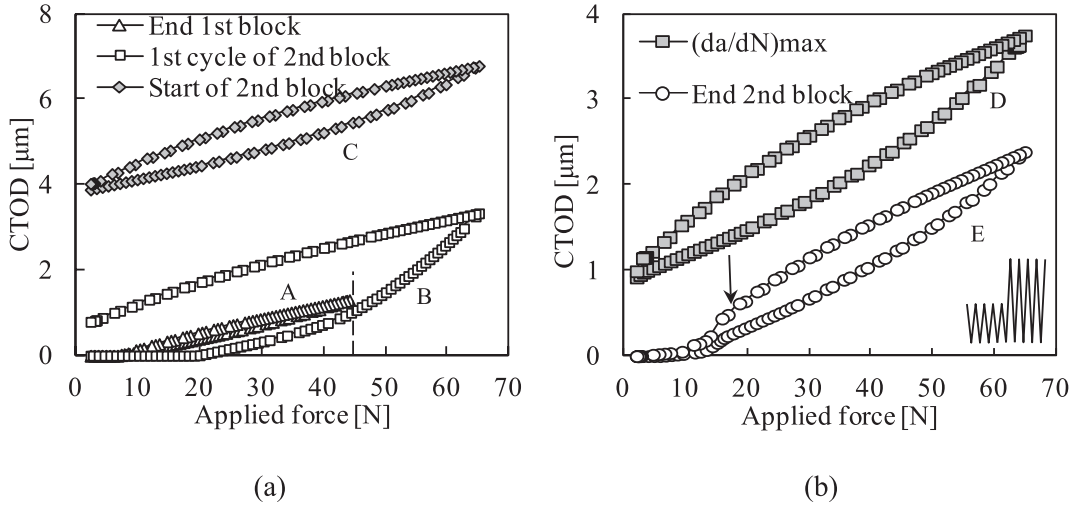

Fig. 12. CTOD plots for the LH_{min} load pattern (Ti6Al4V).

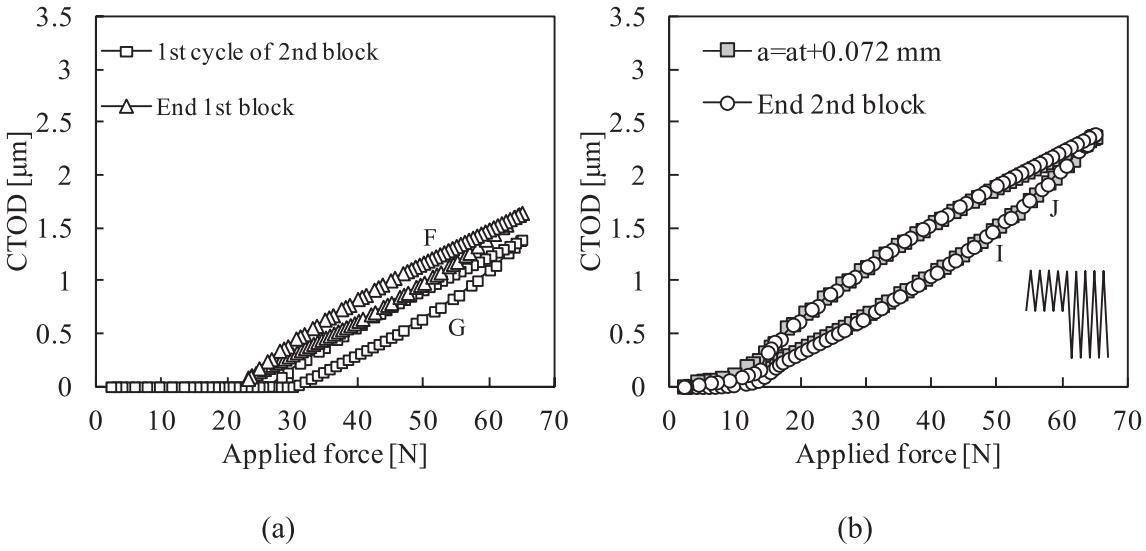

Fig. 13. CTOD plots for the LH_{max} load pattern (Ti6Al4V).

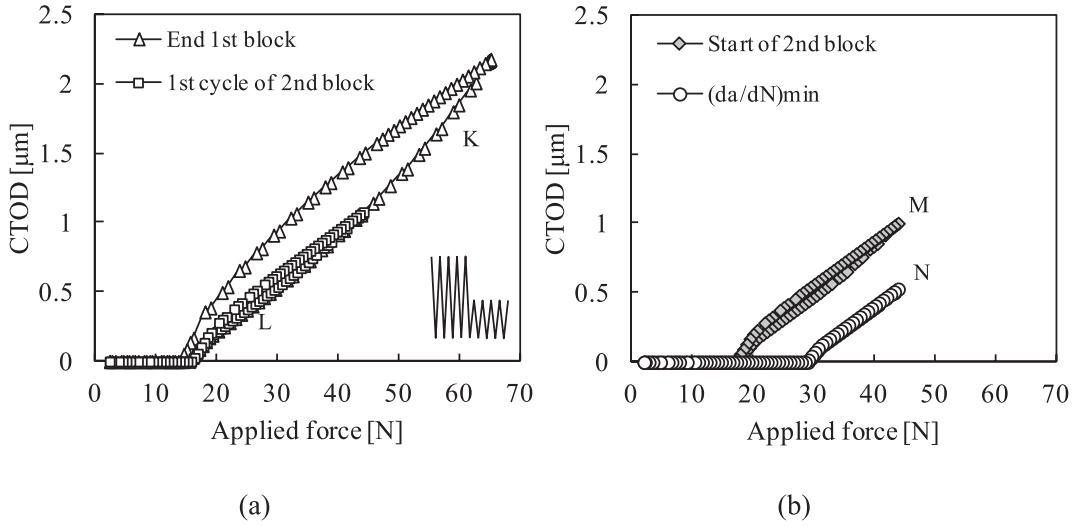

Fig. 14. CTOD plots for the HL_{min} load pattern (Ti6Al4V).

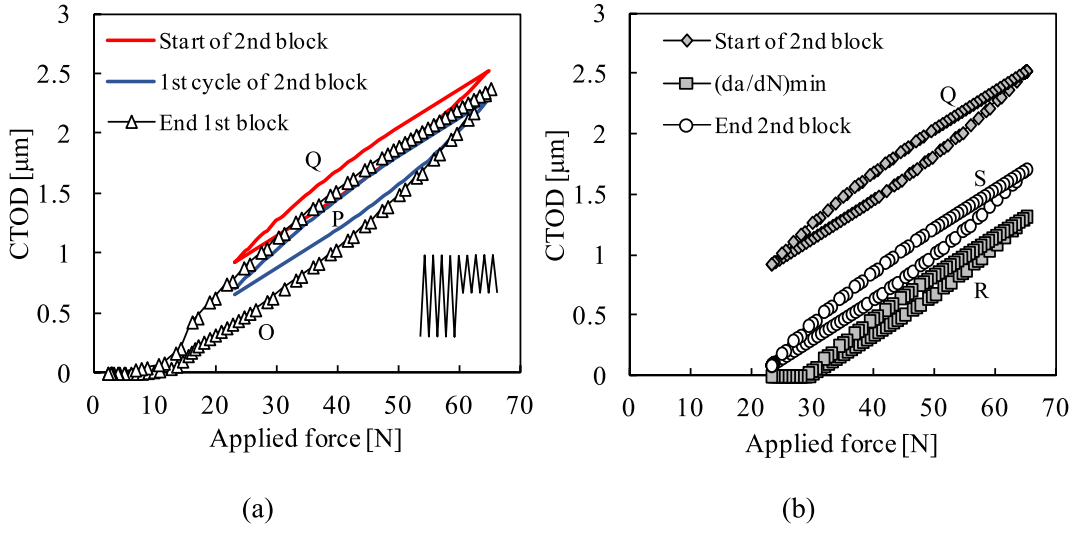

Fig. 15. CTOD plots for the HL_{max} load pattern (Ti6Al4V).

4.3. Crack closure measurements

Previous results show the huge importance of crack closure phenomenon in this context, therefore this phenomenon is now quantified using [38]:

$$U^* = \frac{F_{open} - F_{min}}{F_{max} - F_{min}} \times 100 \quad (4)$$

where F_{open} is the crack opening load. This parameter, which quantifies the fraction of load cycle during which the crack is closed, was evaluated using two different approaches. First, the F_{open} was obtained using the contact status of the first node behind crack tip, i.e. the CTOD measured at a distance of 8 μm behind the crack tip. Alternatively, it was obtained using the evolution of the contact force at the crack flank. In order to ensure the stabilization of the residual plastic wake, the crack closure is evaluated in the load cycle immediately before the crack propagation (nodal release). Note that the crack closure level U^* is directly related with parameter U established by Elber [39] to quantify the fraction of the load cycle over which the crack is open, i.e., U*= (1–U) × 100.

The evolution of the predicted crack closure level evaluated using the CTOD curve is presented in Fig. 16 for the block loading sequences applied to the Ti6Al4V alloy. In the LH_{min} load pattern (Fig. 16a), the crack closure in the steady state regime of the first load block is about 11%, which vanish at the beginning of the second block. Then, it increases progressively until achieve the stable value around 7% in the second load block. Since the first block of the LH_{max} load pattern presents a large stress ratio (R = 0.36), no crack closure was found during the entire loading block. Then, the crack closure starts to increase in the second load block since R = 0.034. The crack closure predicted for the HL_{min} load pattern is presented in Fig. 17b. The stress ratio is relatively low in both load blocks, leading to a sudden increase of the crack closure level in the transition from low to high stress level (see Fig. 14a). Since the crack closure is larger than 65% at the beginning of the second load block, the crack growth stops suddenly (see Fig. 14b). The increase of the stress ratio associated to the second load block in the HL_{max} load pattern yields different levels of crack closure. Indeed, the crack closure starts to increase at the beginning of the second block (achieving 15%) and then decreases until vanish, as shown in Fig. 16b. This trend in the crack closure level is in agreement with the predicted da/dN for the second load block (Fig. 9b), i.e. the FCG rate starts to decrease and then increases until achieve the steady state regime.

Fig. 17 shows crack closure results for the 6082-T6 aluminium alloy. Globally, the crack closure level decreases with the increase of the stress ratio. This explains the trend observed in Fig. 7 for the increase of da/dN with stress ratio. In the first load block, crack closure level decreases from approximately 24% down to 8%. Regarding the second load block, the crack closure level presents the transient regime due to the low-high load block sequence. Nevertheless, it is lower when evaluated from the CTOD in the first node behind the crack tip, particularly for the higher value of stress ratio (R = 0.4). This is a consequence of the partial closure phenomenon, which is not highlighted in the CTOD curve.

The predicted crack flank profile evaluated at the minimum load is presented in Fig. 18 for the situation involving the low–high load block sequence. The transition between blocks is well defined, due to the crack tip blunting. This blunting separates the crack flanks corresponding to the first load block, which are completely separated during the second load block. Partial crack closure occurs in the second load block since the CTOD in the two nodes behind the crack tip is positive, as shown in Fig. 18. During the first load block, the crack closure extension increases during the crack propagation up to approximately 0.45 mm, which corresponds to the extent of the transient regime in the FCG rate (Fig. 6a). The same behaviour is observed in the second load block, where the crack closure extension increases up to about 0.6 mm (Fig. 18). Therefore, the steady state of the FCG rate in the second load block is achieved after 0.6 mm of crack propagation.

5. Conclusions

The effect of variable amplitude block loading on fatigue crack growth (FCG) was numerically evaluated using different low–high and high-low sequences. The numerical model was based on the cumulative plastic strain at the crack tip. The main conclusions are:

- The numerical model was validated with experimental results for MT specimens made of 6082-T6 aluminium alloy. A good agreement was found between the numerical predictions and experimental results, which validated the fundamental assumption that FCG is linked to cyclic plastic deformation at the crack tip. Some numerical/experimental differences at the beginning of the second block may be explained by the relatively small number of measurement points in the experimental work. In High-Low block sequence the extent of retardation is underestimated by the numerical model.
- In both numerical and experimental studies, it was found that the LH_{min} sequence produces an acceleration of crack growth rate, above the steady state level expected for the high block, followed by a gradual reduction to the steady state da/dN value. The increase of ΔK jump extends the transient regime, while the increase of stress ratio produces a global increase of da/dN. In HL_{min} sequences, there is a fast and strong reduction of FCG rate, followed by a progressive increase to the steady state da/dN corresponding to the second block.

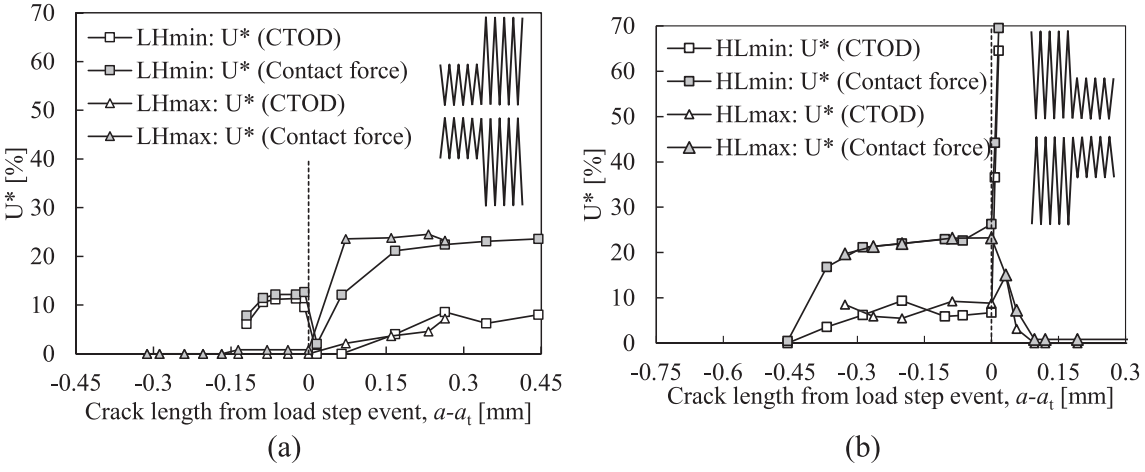

Fig. 16. Evolution of the crack closure level for different block loading (Ti6Al4V): (a) Low-High load blocks; (b) High-Low load blocks.

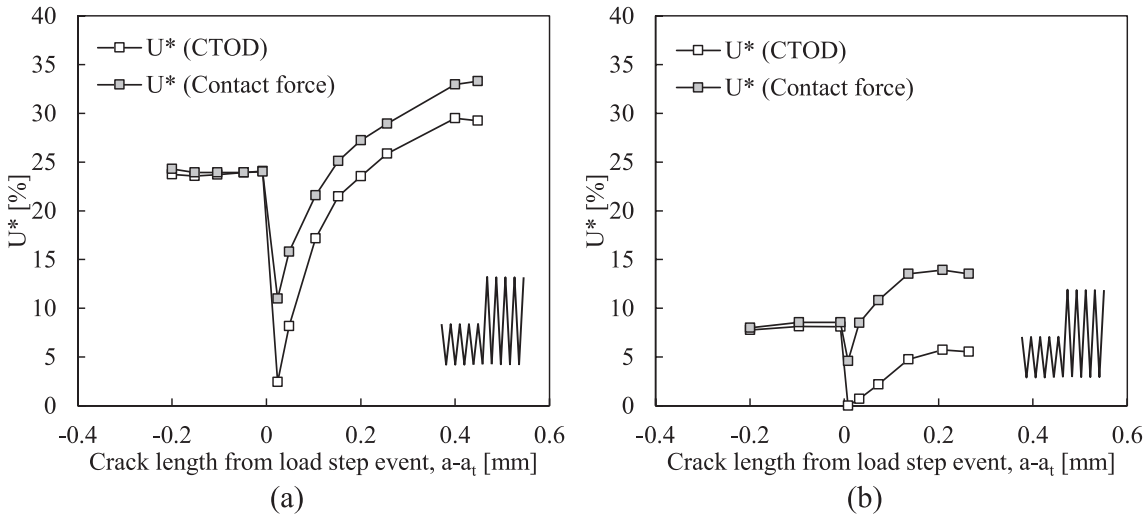

Fig. 17. Influence of the stress ratio on the crack closure level in low–high load blocks with $\Delta K_1 = 6$ MPa.m$^{1/2}$ and $\Delta K_2 = 9$ MPa.m$^{1/2}$: (a) R = 0.05; (b) R = 0.4. (AA6082-T6).

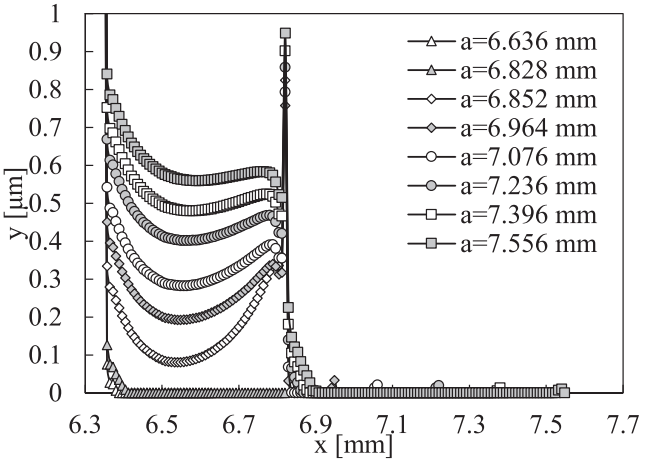

Fig. 18. Evolution of the predicted crack flank profile evaluated at the minimum load in the low–high load block with $\Delta K_1 = 9$ MPa.m$^{1/2}$ and $\Delta K_2 = 12$ MPa.m$^{1/2}$ (R = 0.05).

The transient region is more extensive than that observed for the LH_{min} sequence. If the load reduction is strong, the crack is arrested.

- The influence of crack closure on the predicted FCG rate was highlighted by removing numerically the contact of crack flanks. The transient behavior observed between loading blocks of different amplitude is strongly reduced or vanishes when the contact is neglected. For load blocks with high values of stress ratio, the predicted FCG rate in steady state regime is approximately the same considering or neglecting the contact of the crack flanks. On the other hand, for low values of stress ratio, the predicted FCG rate is lower when the contact of the crack flanks is considered, which is related with the effective load range.
- The main mechanisms involved in the transient effect produced by load blocks are:
  - crack closure which explains: the initial decrease of da/dN at the beginning of simulation, which is due to the formation of residual plastic wake; the peak of da/dN in LH_{max} load pattern; the crack arrest in HLmin load pattern; the decrease of the influence of contact and non-contact conditions with the increase of R.
  - material hardening in LH_{min} pattern. The lack of hardening when the first load cycle of the second block rises above the maximum load of the first block is responsible for crack tip blunting which eliminates totally or partially the load history.
  - partial crack closure in high-low load blocks. The plastic wake of the first load block has an effect on the crack propagation of the second block and may even stop the propagation.

Declaration of Competing Interest

The authors declare that they have no known competing financial interests or personal relationships that could have appeared to influence the work reported in this paper.

Acknowledgements

The authors gratefully acknowledge the financial support of the Portuguese Foundation for Science and Technology (FCT) under the project with reference PTDC/EME-EME/31657/2017 and by European Regional Development Fund (ERDF) through the Portugal 2020 program and the Centro 2020 Regional Operational Programme (CENTRO-01-0145-FEDER-031657). This research is also sponsored by the project UIDB/00285/2020.

References

[1] Heuler P, Klatschke H. Generation and use of standardised load spectra and load–time histories. Int J Fatigue 2005;27(8):974–90.
[2] de Jonge JB, Schutz D, Lowak H, Schijve J. A Standardized Load Sequence for Flight Simulation Tests on Transport Aircraft Wing Structures, NLR TR 73029U. The Netherlands: National Aerospace Laboratory (NLR); 1973.
[3] Christensen RH. Fatigue crack, fatigue damage and their detection, Metal fatigue. New York: MacGraw-Hill; 1959.
[4] Tvergaard V. Effect of underloads or overloads in fatigue crack growth by crack-tip blunting. Eng Fract Mech 2006;73(7):869–79.
[5] Schijve J, Broek D. The result of a test program based on a gust spectrum with variable amplitude loading. Aircraft Eng 1962;34:314–6.
[6] Xiao L, Ye D, Chen C, Liu J, Zhang L. Instrumented indentation measurements of residual stresses around a crack tip under single tensile overloads. Int J Mech Sci 2014;78:44–51.
[7] Jones RE. Fatigue crack growth retardation after single-cycle peak overload in Ti–6Al–4V titanium alloy. Eng Fract Mech 1973;5(3):585–604.
[8] Kermanidis AT, Pantelakis SG. Prediction of crack growth following a single overload in aluminum alloy with sheet and plate microstructure. Eng Fract Mech 2011;78(11):2325–37.
[9] Suresh S. Micromechanisms of fatigue crack growth retardation following overloads. Eng Fract Mech 1983;18(3):577–93.
[10] Borrego LP, Ferreira JM, Pinho da Cruz JM, Costa JM. Evaluation of overload effects on fatigue crack growth and closure. Eng Fract Mech 2003;70(11):1379–97.
[11] Vasco-Olmo JM, Díaz FA, James MN, Yang B. Crack tip plastic zone evolution during an overload cycle and the contribution of plasticity-induced shielding to crack growth rate changes. Fat Fract Eng Mater Struct 2018;41:2172–86.

[12] Neto DM, Borges MF, Antunes FV, Jesus J. Mechanisms of fatigue crack growth in Ti-6Al-4V alloy subjected to single overloads. Theor Appl Fract Mech 2021;114:103024.
[13] Ward-Close CM, Blom AF, Ritchie RO. Mechanisms associated with transient fatigue crack growth under variable amplitude loading: an experimental and numerical study. Eng Fract Mech 1989;32(4):613–38.
[14] Sehitoglu H, Mcdiarmid D. The effect of load step-down on fatigue crack arrest and retardation. Int J Fatigue 1980;2(2):55–60.
[15] Borrego L, Ferreira J, Costa J. Partial crack closure under block loading. Int J Fatigue 2008;30(10-11):1787–96.
[16] Remadi A, Bahloul A, Bouraoui C. Prediction of fatigue crack growth life under variable-amplitude loading using finite element analysis. CR Mec 2019;347(8):576–87.
[17] Noroozi A, Glinka G, Lambert S. A two parameter driving force for fatigue crack growth analysis. Int J Fatigue 2005;27(10-12):1277–96.
[18] Haier JWAE. Fatigue Crack Growth Thresholds—The influence of Young's Modulus and Fracture Surface Roughness. Int J Fatigue 2018;117:163–79.
[19] Hamam R, Pommier S, Bumbieler F. Mode I Fatigue Crack Growth under Biaxial Loading. Int J Fatigue 2005;27(10-12):1342–6.
[20] Pippan R, Grosinger W. Fatigue crack closure: From LCF to small scale yielding. Int J Fatigue 2013;46:41–8.
[21] Antunes FV, Serrano S, Branco R, Prates P. Fatigue crack growth in the 2050–T8 aluminium alloy. Int J Fatigue 2018;115:79–88.
[22] Savaidis G, Savaidis A, Zerres P, Vormwald M. Mode I fatigue crack growth at notches considering crack closure. Int J Fatigue 2010;32(10):1543–58.
[23] Rozumek D. Influence of the slot inclination angle in FeP04 steel on fatigue crack growth under tension. Mater Des 2009;30(6):1859–65.
[24] Rozumek D, Macha E. Elastic–plastic fatigue crack growth in 18G2A steel under proportional bending with torsion loading. Fat Fract Eng Mater Struct 2006;29(2):135–44.
[25] Klingbeil N. A total dissipated energy theory of fatigue crack growth in ductile solids. Int J Fatigue 2003;25(2):117–28.
[26] Borges MF, Neto DM, Antunes FV. Numerical simulation of fatigue crack growth based on accumulated plastic strain. Theor Appl Fract Mech 2020;108:102676.
[27] Ould Chikh B, Imad A, Benguediab M. Influence of the cyclic plastic zone size on the propagation of the fatigue crack in case of 12NC6 steel. Comput Mater Sci 2008;43(4):1010–7.
[28] Menezes LF, Teodosiu C. Three-dimensional numerical simulation of the deep-drawing process using solid finite elements. J Mater Process Tech 2000;97(1-3):100–6.
[29] ASTM E647-15: Standard test method for measurement of fatigue crack growth rates, Philadelphia: American Society for Testing and Materials (2015) ASTM.
[30] Borges MF, Neto DM, Antunes FV. Revisiting Classical Issues of Fatigue Crack Growth Using a Non-Linear Approach, Materials 2020;13:5544.
[31] Antunes FV, Rodrigues SM, Branco R, Camas D. A numerical analysis of CTOD in constant amplitude fatigue crack growth. Theor Appl Fract Mech 2016;85:45–55.
[32] Ferreira FF, Neto DM, Jesus JS, Prates PA, Antunes FV. Numerical Prediction of the Fatigue Crack Growth Rate in SLM Ti-6Al-4V Based on Crack Tip Plastic Strain. Metals 2020;10:1133.
[33] Ng'ang'a SP, James MN. Variable amplitude loading in En8 (080M40) steel: a detailed experimental study of crack growth. Fat Fract Eng Mater Struct 1996;19(2-3):207–16.
[34] Micone N, De Waele W. Experimental evaluation of block loading effects on fatigue crack growth in offshore structural steels. Mar struct 2019;64:463–80.
[35] Neto DM, Borges MF, Antunes FV, Sunder R. Numerical analysis of SuperBlock2020 loading sequence. Eng Fract Mech 2022;260:108178.
[36] Paris PC, Tada H, Donald JK. Service load fatigue damage - a historical perspective. Int J Fatigue 1999;21:S35–46.
[37] Kujawski D. Enhanced model of partial crack closure for correlation of R-ratio effects in aluminum alloys. Int J Fatigue 2001;23(2):95–102.
[38] Borges MF, Antunes FV, Prates PA, Branco R, Cruces AS, Lopez-Crespo P. Effect of kinematic hardening parameters on fatigue crack growth. Theor Appl Fract Mech 2020;106:102501.
[39] Wolf E. Fatigue crack closure under cyclic tension. Engng Fracture Mechanics 1970;2(1):37–45.